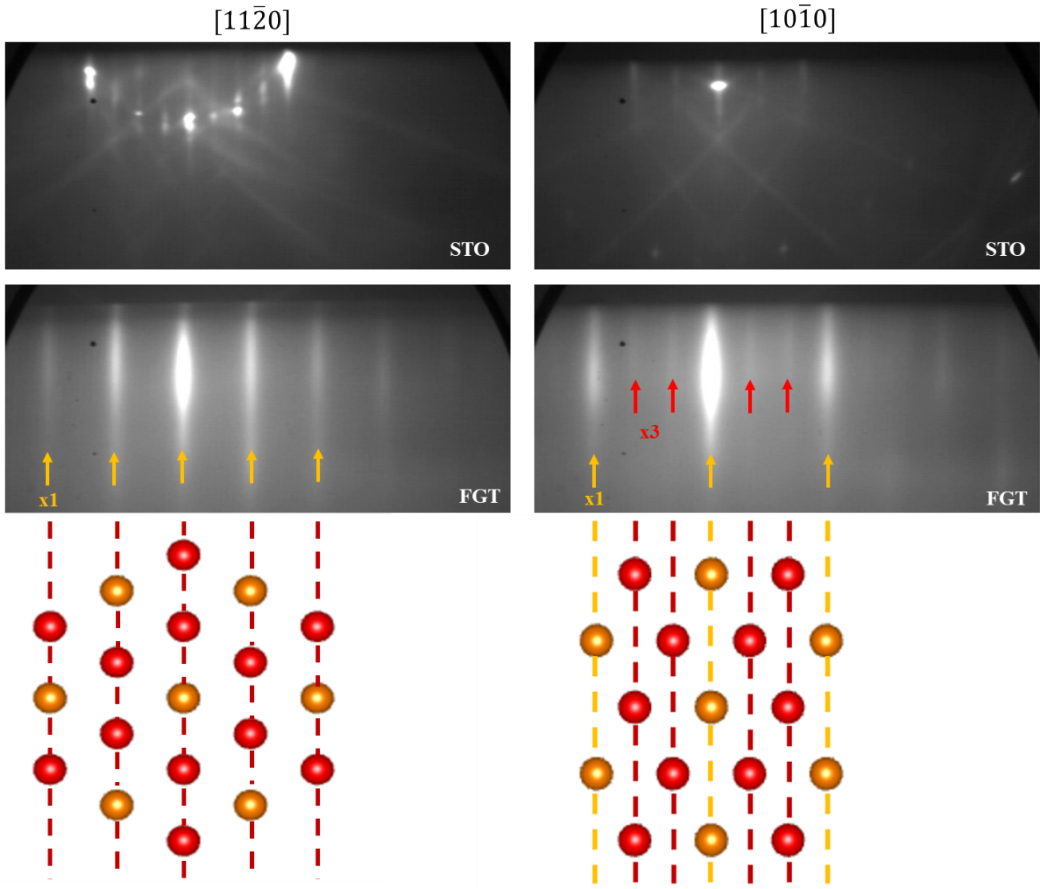

Fig. S1 RHEED diffraction patterns before and after the deposition for 9 nm thick FGT. Schematic below illustrates the (√3 ×√3) R30◦ superstructure. Red arrows indicate the x3 reconstruction.

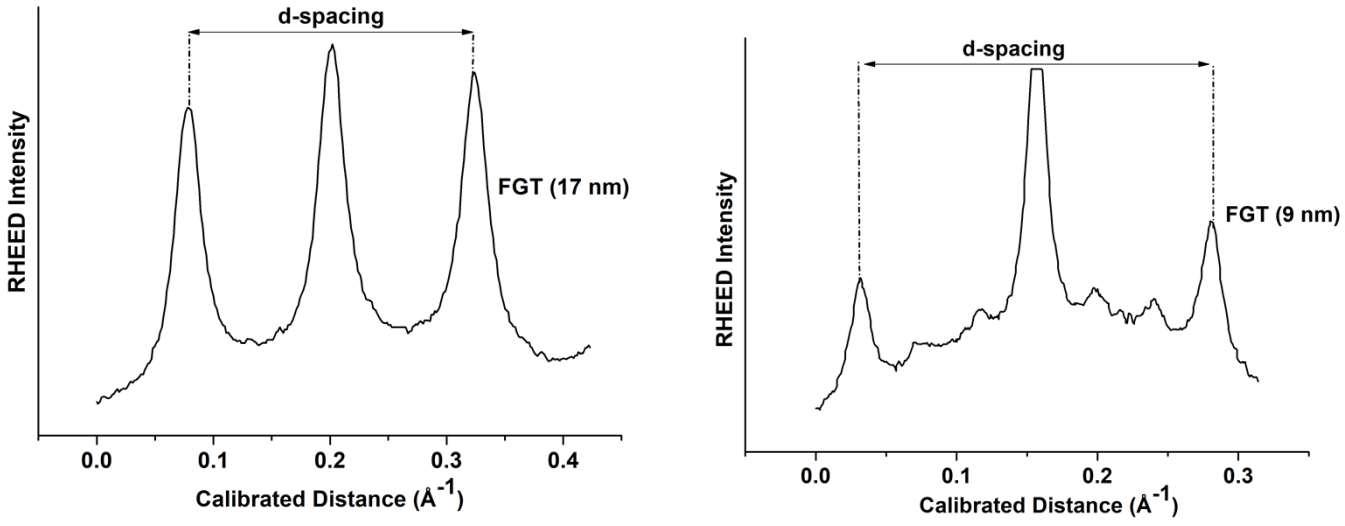

(a) (b)

Fig. S2 Line scans of the RHEED patterns for (a) 17 nm thick FGT and (b) 9 nm thick FGT.

EDS analysis has been carried out in order to ensure the stoichiometry. Quantitative analysis was performed using the EDAX Genesis software and the ZAF correction method. Fig. S3

shows representative EDS spectra. From EDS analysis the composition for the sample is close to the nominal values, in consensus with the structural characterization.

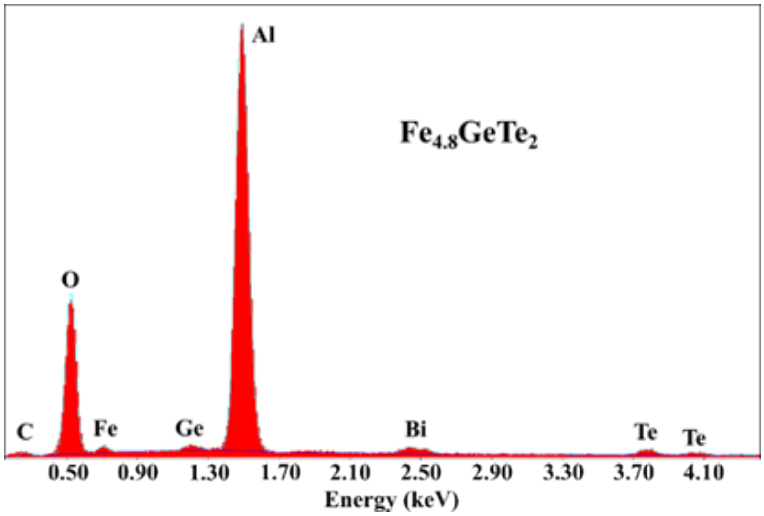

Fig. S3 Representative EDS spectra for 17 nm thick FGT/Bi_2Te_3.

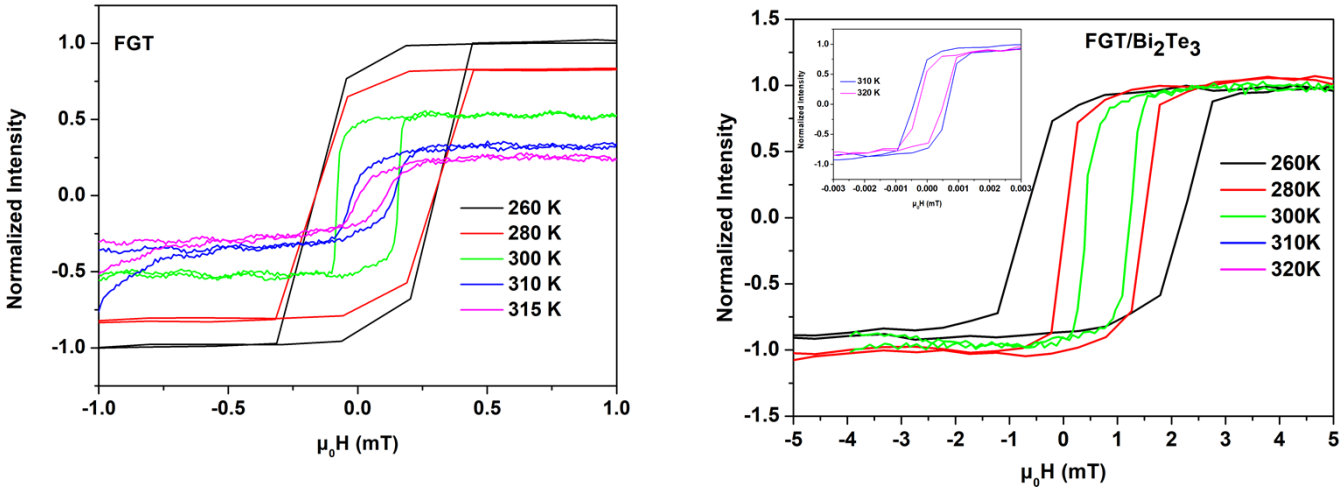

(a) (b)

Fig. S4 MOKE hysteresis loops for 9 nm thick FGT (left) and FGT/Bi_2Te_3 (right) heterostructures.

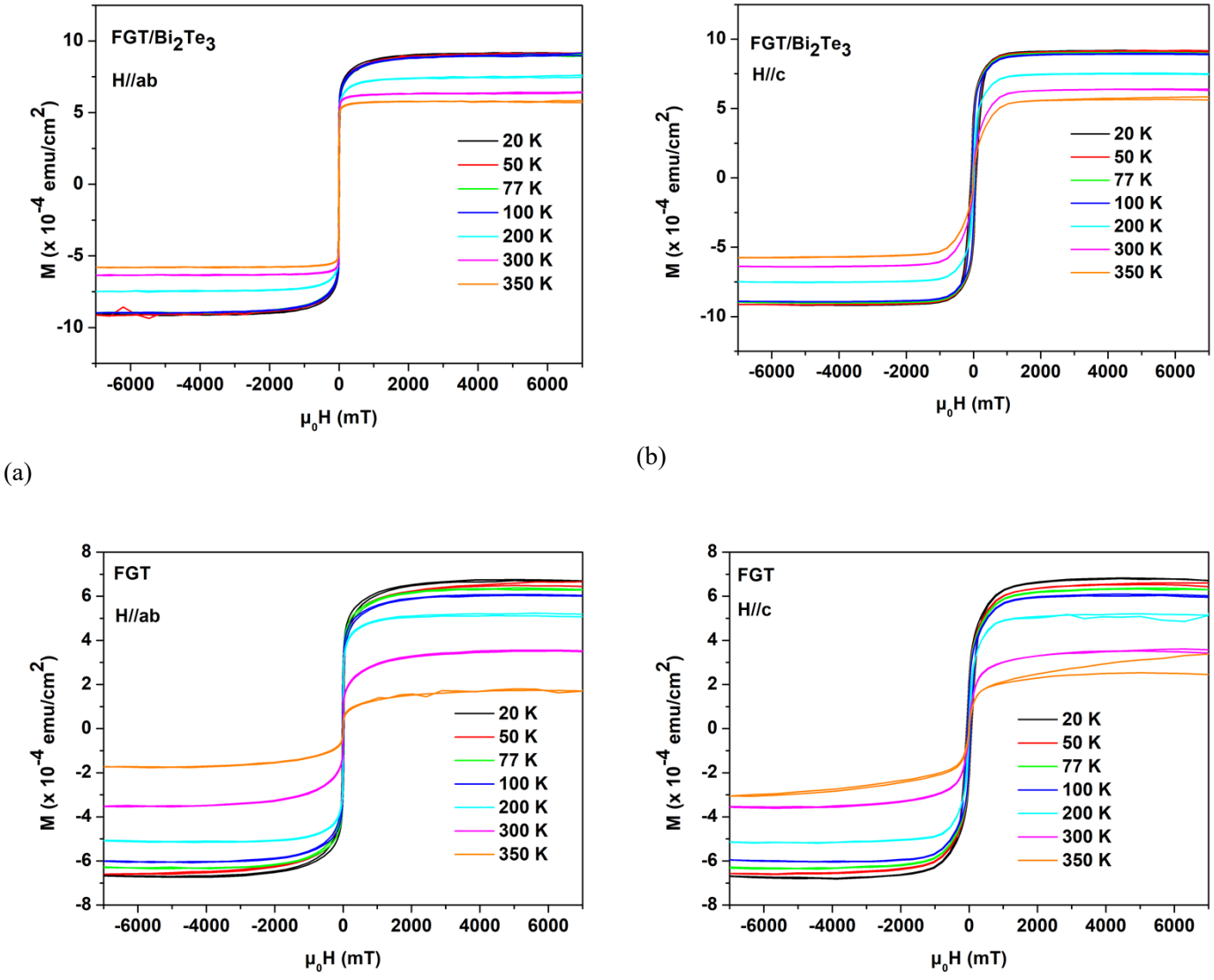

Fig. S5 SQUID measurements for 17 nm thick FGT/Bi_2Te_3 (a) in plane and (b) out of plane component and 17 nm thick FGT (c) in plane and (d) out of plane component.

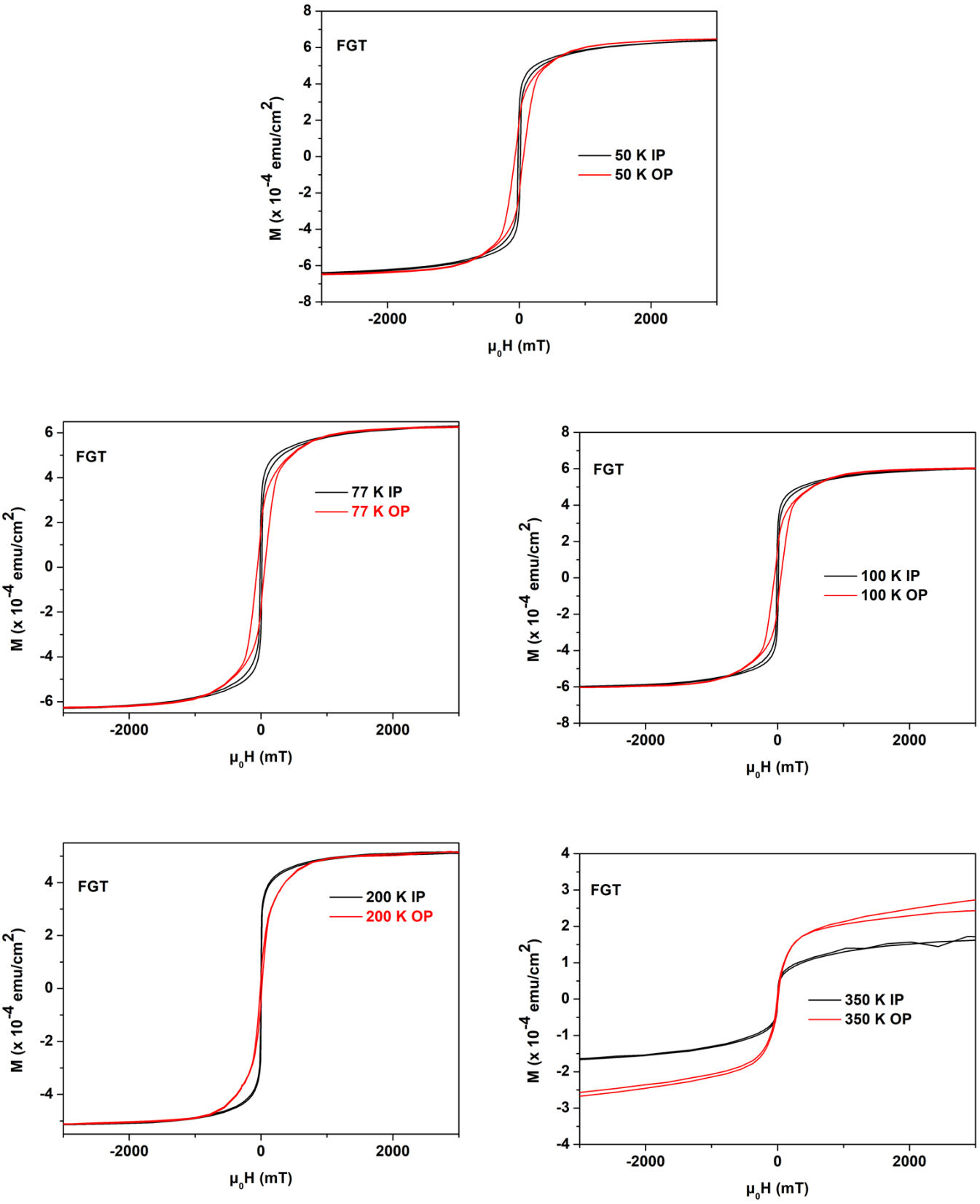

Fig. S6 Comparison of in plane and out of plane component by SQUID measurements for 17 nm thick FGT.

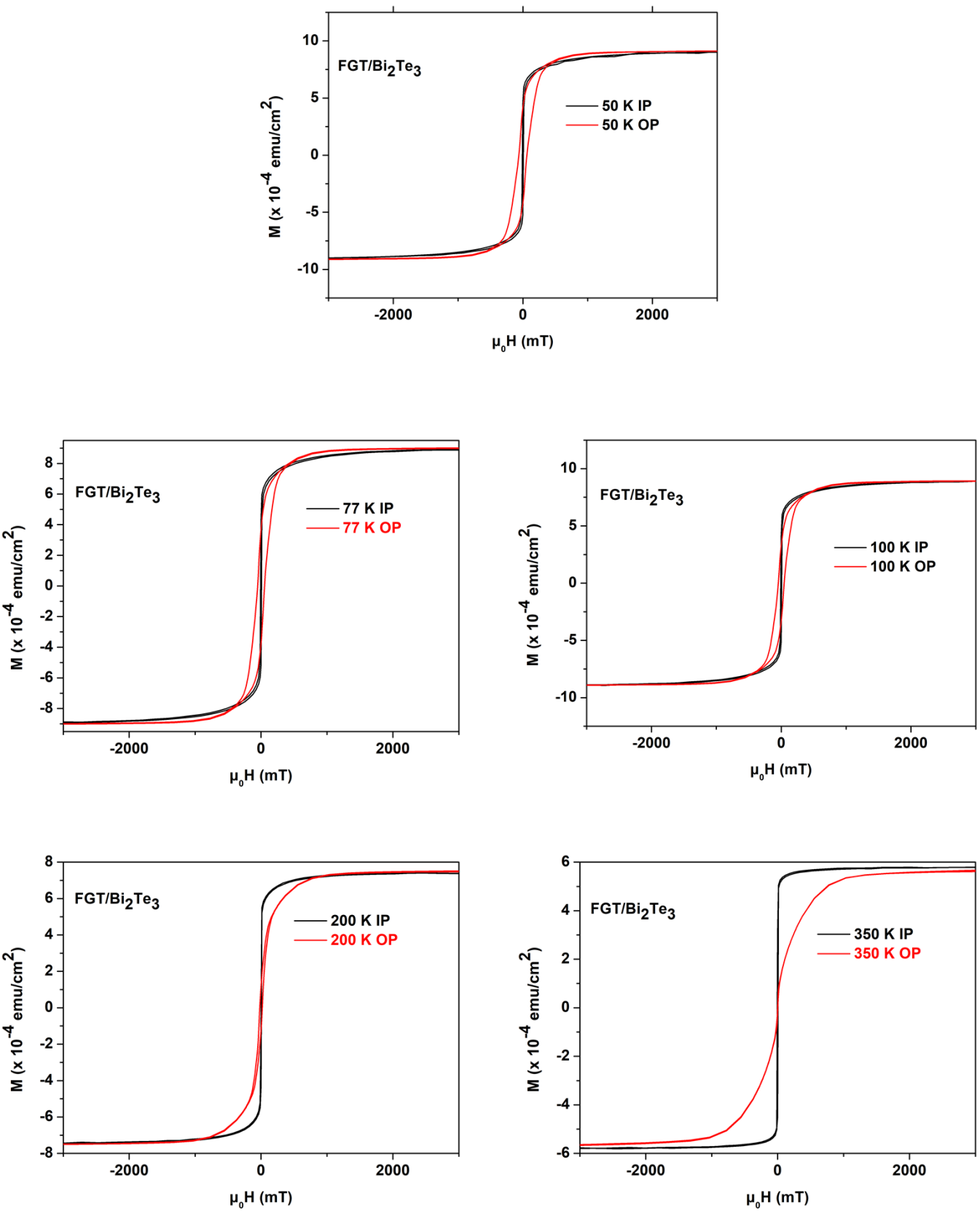

Fig. S7 Comparison of in plane and out of plane component by SQUID measurements for 17 nm thick FGT/Bi_2Te_3.

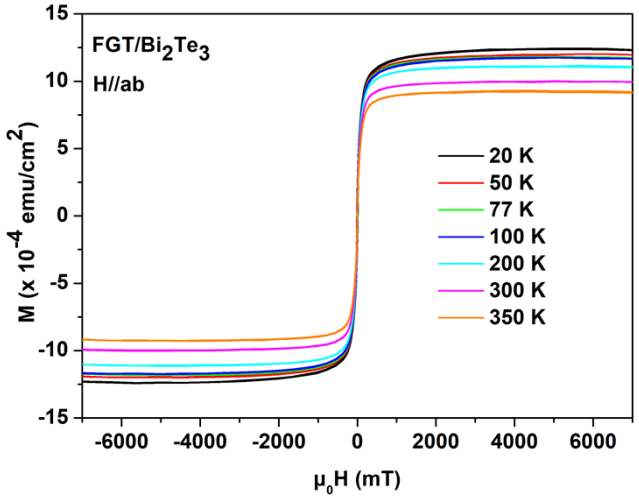

(a)

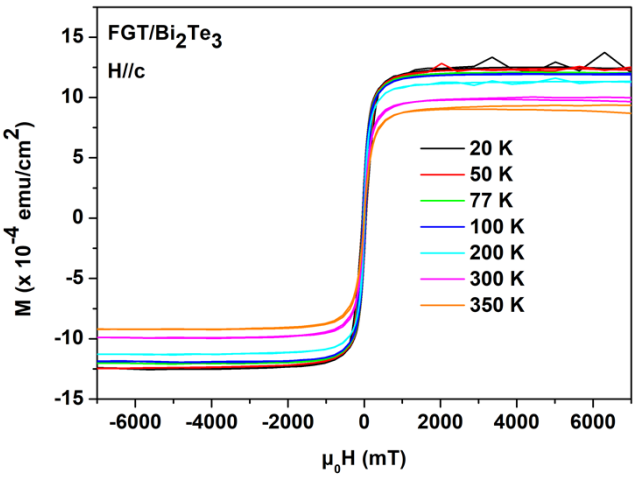

(b)

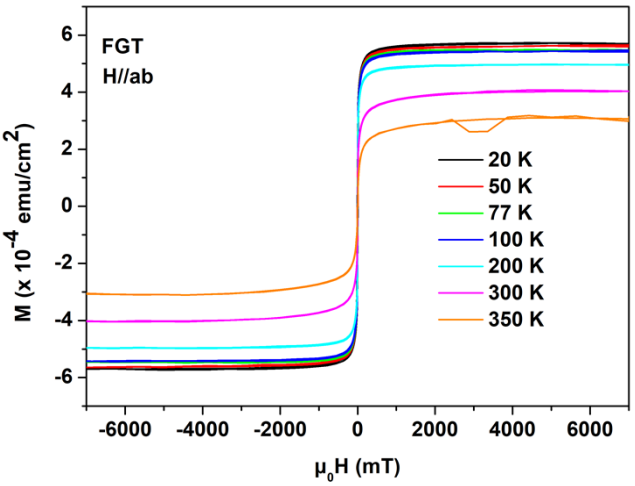

(c)

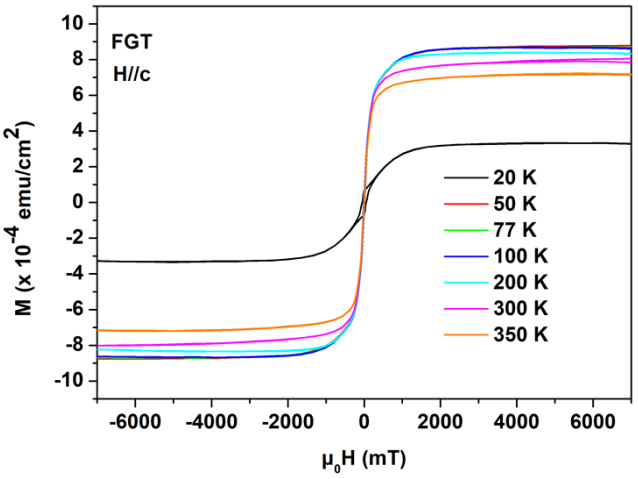

(d)

Fig. S8 SQUID measurements for 9 nm thick FGT/Bi_2Te_3 (a) in plane and (b) out of plane component and 9 nm thick FGT (c) in plane and (d) out of plane component.

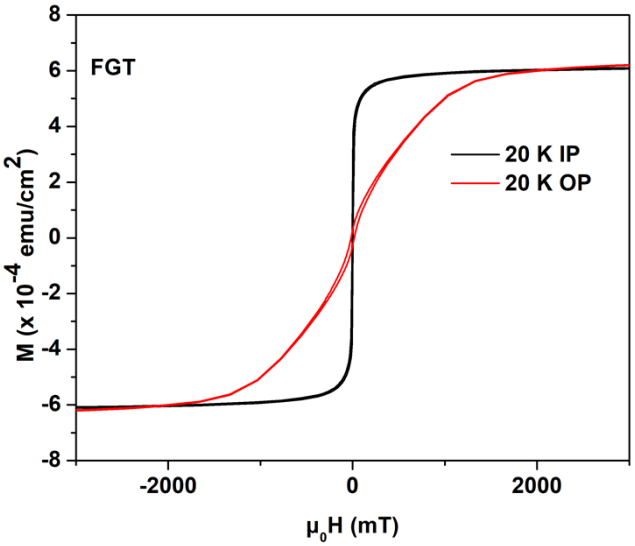
FGT
20 K IP
20 K OP
M (x 10^-4 emu/cm^2)
μ0H (mT)
8
6
4
2
0
-2
-4
-6
-8
-2000
0
2000

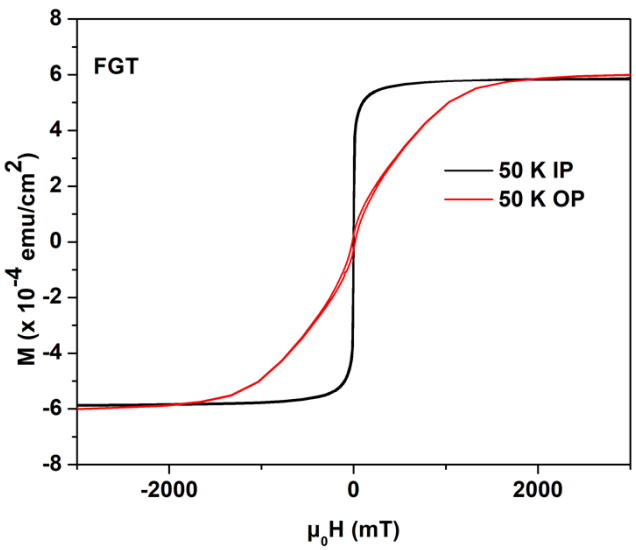
FGT
50 K IP
50 K OP
M (x 10^-4 emu/cm^2)
μ0H (mT)
8
6
4
2
0
-2
-4
-6
-8
-2000
0
2000

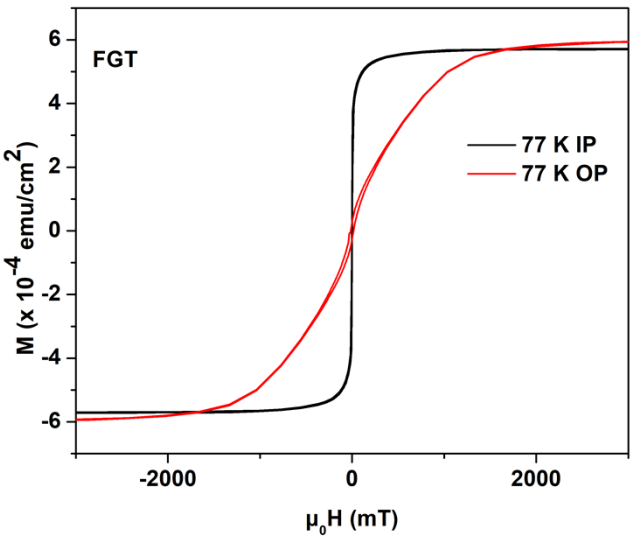
FGT
77 K IP
77 K OP
M (x 10^-4 emu/cm^2)
μ0H (mT)
6
4
2
0
-2
-4
-6
-2000
0
2000

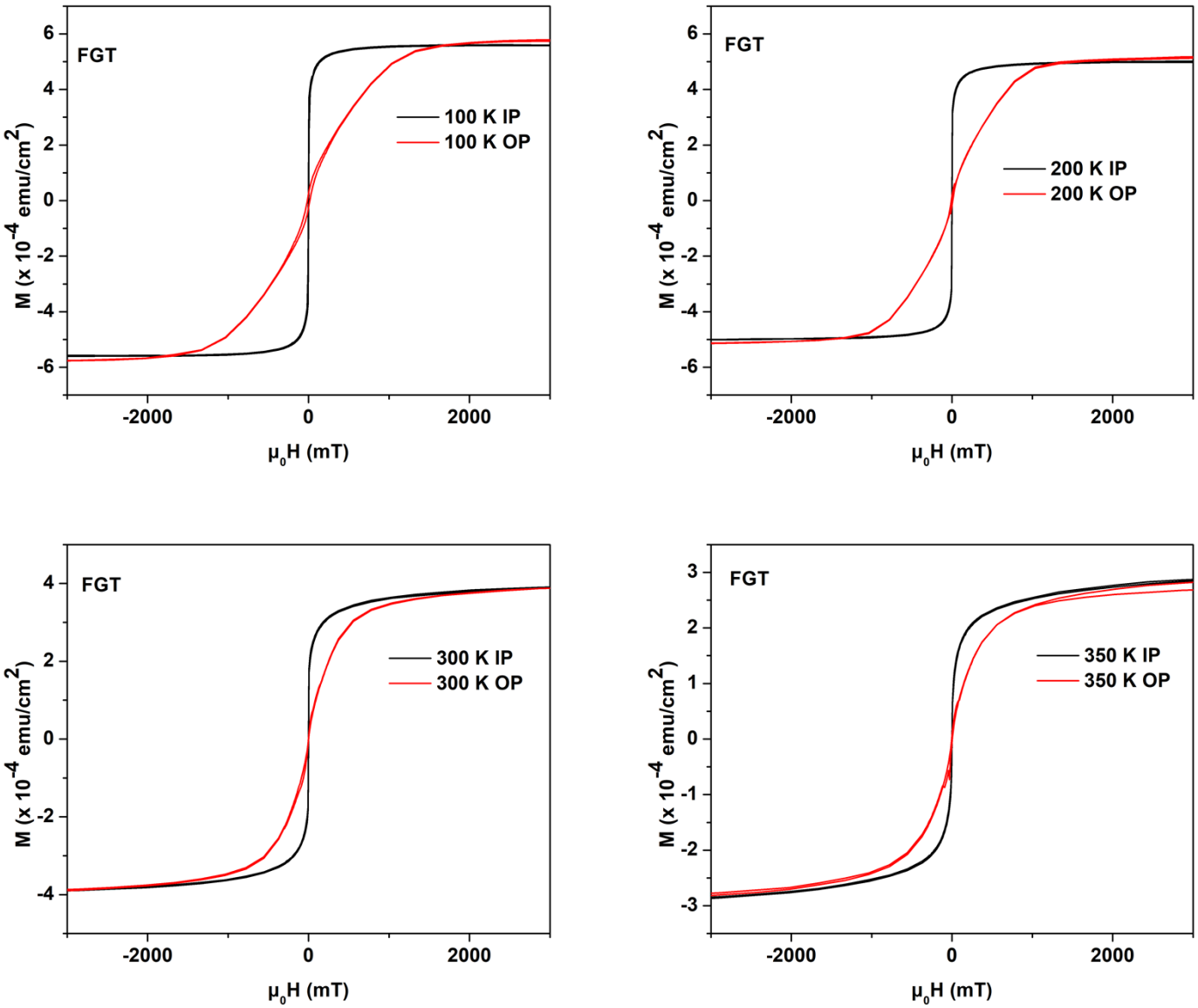

Fig. S9 Comparison of in plane and out of plane component by SQUID measurements for 9 nm thick FGT.

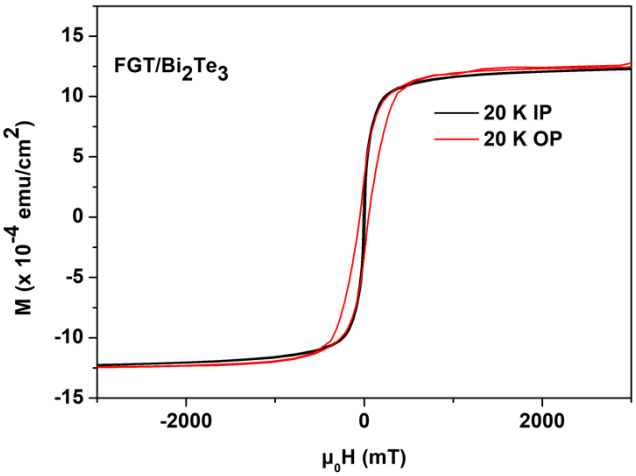
FGT/Bi2Te3
20 K IP
20 K OP
M (x 10-4 emu/cm2)
μ0H (mT)

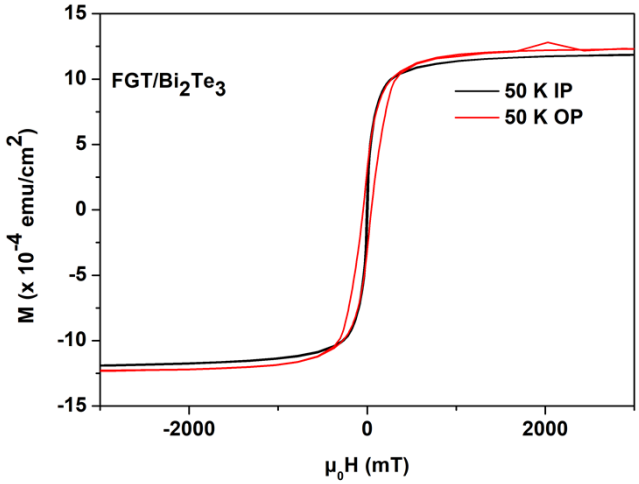
FGT/Bi2Te3
50 K IP
50 K OP
M (x 10-4 emu/cm2)
μ0H (mT)

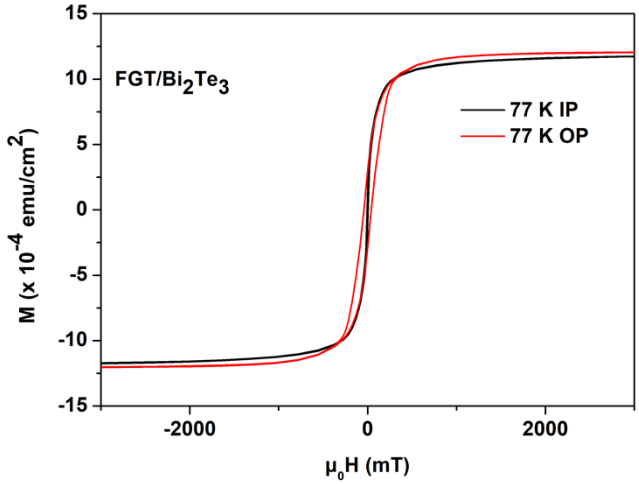
FGT/Bi2Te3
77 K IP
77 K OP
M (x 10-4 emu/cm2)
μ0H (mT)

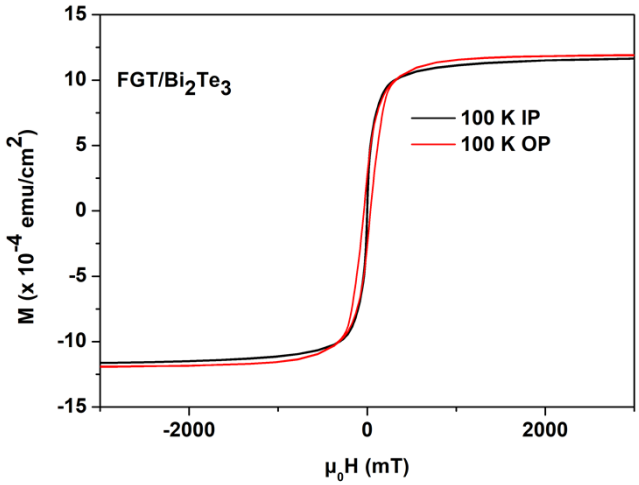
FGT/Bi2Te3
100 K IP
100 K OP
M (x 10-4 emu/cm2)
μ0H (mT)

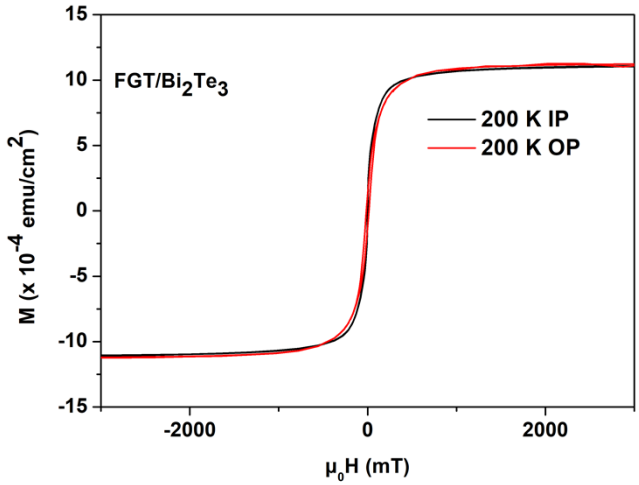
FGT/Bi2Te3
200 K IP
200 K OP
M (x 10-4 emu/cm2)
μ0H (mT)

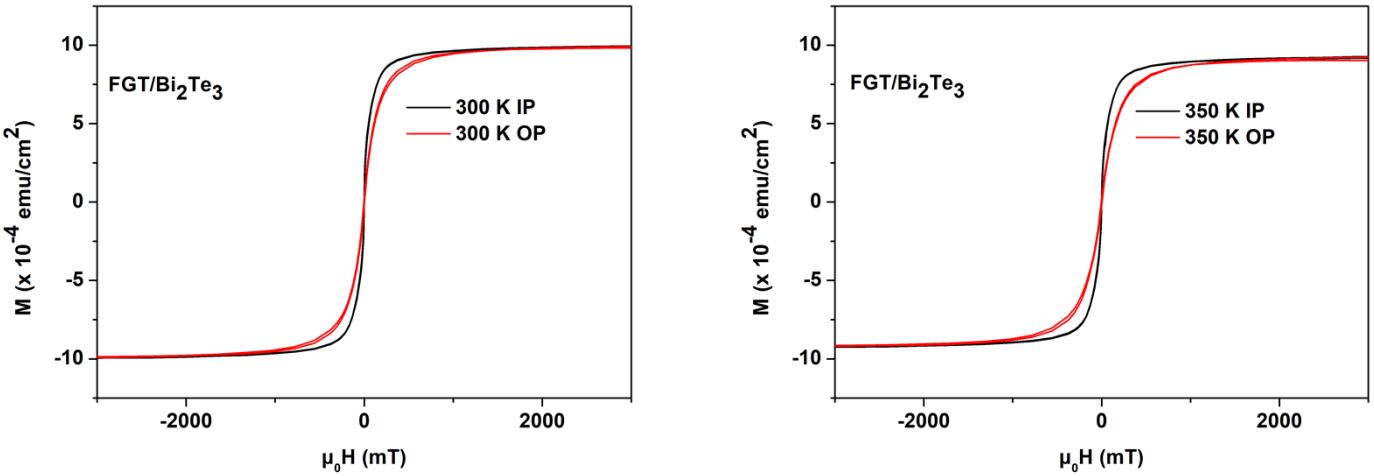

Fig. S10 Comparison of in plane and out of plane component by SQUID measurements for 9 nm thick FGT/Bi_2Te_3.

For the thinner 9 nm FGT films, the FGT heterostructure has clear OP anisotropy from 350 K down to 50 K (Fig. S9). At 20 K it is observed a change from OP to IP anisotropy for the FGT (Fig. S9). On the other hand, the presence of Bi_2Te_3 changes the anisotropy of the FGT film, strengthening the IP anisotropy (Fig. S10). More specifically, the FGT/Bi_2Te_3 has an IP anisotropy above 200 K and below 200 K the sample is almost isotropic regarding the IP and OP anisotropy (Fig. S10), as was the case of 17 nm FGT/Bi_2Te_3.

The lattice constant of Fe_5GeTe_2 monolayer was kept to the experimental values of $\alpha = 4.0376$ Å and the Bi_2Te_3 has assumed the Fe_5GeTe_2 lattice constant. Relaxation of the ion positions of the Fe_5GeTe_2/Bi_2Te_3 heterostructure revealed that the most stable configuration is the one depicted in Fig. S11.

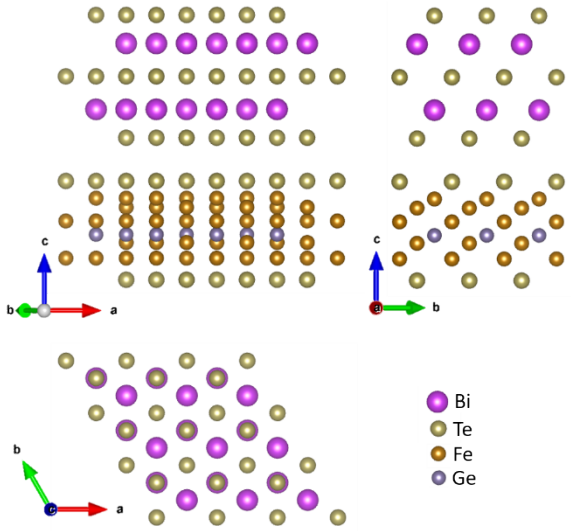

Fig. S11 The structure of the FGT/Bi_2Te_3 heterostructure. Side view (up) and top view (down).

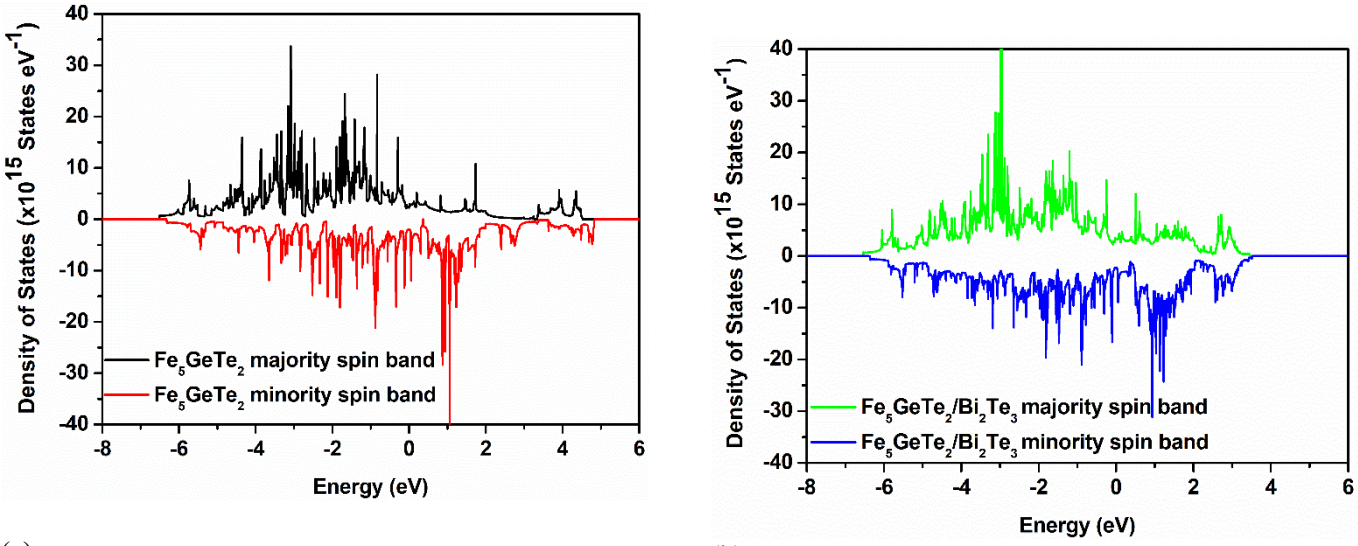

(a) (b)

Fig. S12 (a) Spin resolved density of states of FGT (black and red lines) and (b) FGT/Bi_2Te_3 (green and blue lines).

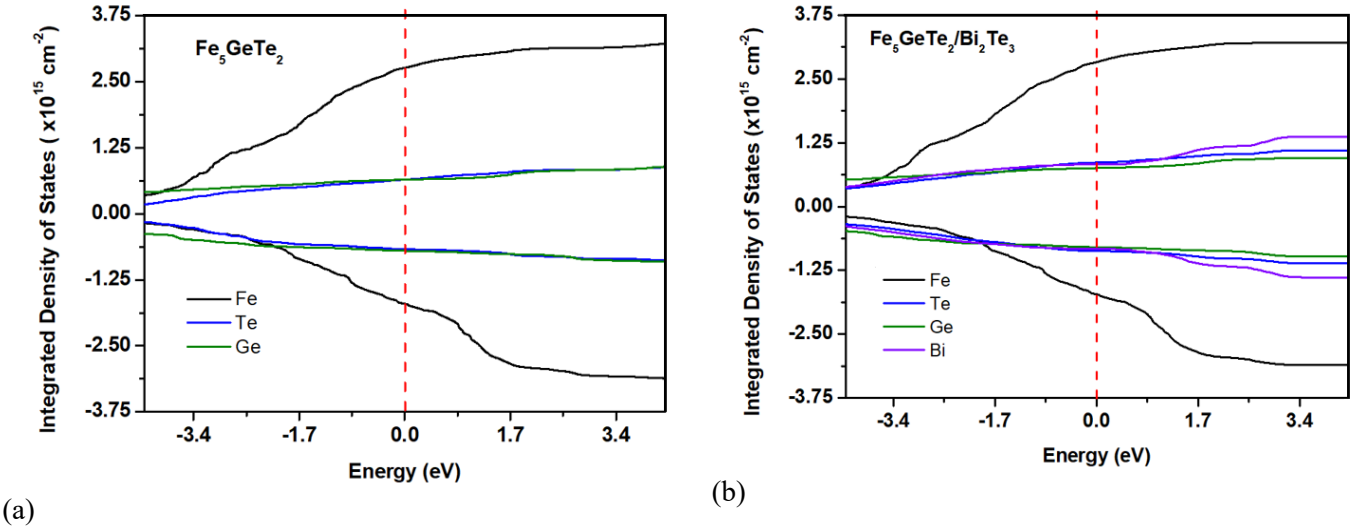

(a) (b)

Fig. S13 Projection of the Integrated Density of states on each element of the FGT (a) and FGT/Bi_2Te_3 (b). The red dashed line indicates the Fermi Level.

BFMR and cavity-FMR measurements were performed on the thin FGT and FGT/Bi_2Te_3 samples to investigate on their magnetization dynamic properties [2], [3]. Fig. S13 (a) displays the Kittel curves acquired in the IP configuration for the the FGT sample (black squares), where the resonant RF-frequency exciting the system f_{res} is plotted as a function of the resonant magnetic field H_{res}. The red solid line represents the fit of the acquired data using the Kittel model for the IP geometry, which is described by the following Eq. (1).

$$f_{res} = \frac{\gamma}{2\pi}\sqrt{H_{res}\left(H_{res} + 4\pi M_{eff}\right)} \tag{1}$$

where γ is the gyromagnetic ratio and M_{eff} the effective magnetization. $\gamma = g\frac{e}{2m_e}\left[\frac{Hz}{Oe}\right]$, where e and m_e are the charge and the mass of the electron, and g is the Landè g-factor, a quantity which links the electronic angular and spin momenta [2]. From the fit of the data in Fig. S13

(a), $\gamma = 1.96 \pm 0.06 \cdot 10^7 \frac{Hz}{Oe}$ $(g \sim 2.23 \pm 0.07)$ and $M_{eff}^{FGT} = 260 \pm 32 \frac{emu}{cm^3}$. M_{eff} can be written as $4\pi M_{eff} = 4\pi M_s - H_k = 4\pi M_s - \frac{2K_{eff}}{M_s}$, where M_s, H_k and K_{eff} are the saturation magnetization, the magnetic anisotropy field and the effective magnetic anisotropy constant, respectively. The M_{eff} value extracted from the fit is lower than M_s obtained from the SQUID measurement acquired at 300 K, thus indicating that the contribution of the out-of-plane anisotropy is not negligible for this material. Indeed, from the extracted values, we obtained the positive value $K_{eff} = 5.1 \cdot 10^5 \frac{erg}{cm^3}$. The obtained quantities turned out to be fully compatible with those reported in [1] of the main text. In Fig. S13 (b), the linewidth ΔH of the BFMR signal is plotted as a function of f_{res} and, according to Eq. (2) in the main text, the values of the damping constant α and the inhomogeneous broadening ΔH_0 can be found. From the linear fit (red solid line) of the datasets reported in Fig. S13 (b), we obtained $\alpha^{FGT} = (51 \pm 6) \cdot 10^{-3}$, $\Delta H_0^{FGT} = 80 \pm 55\ Oe$.

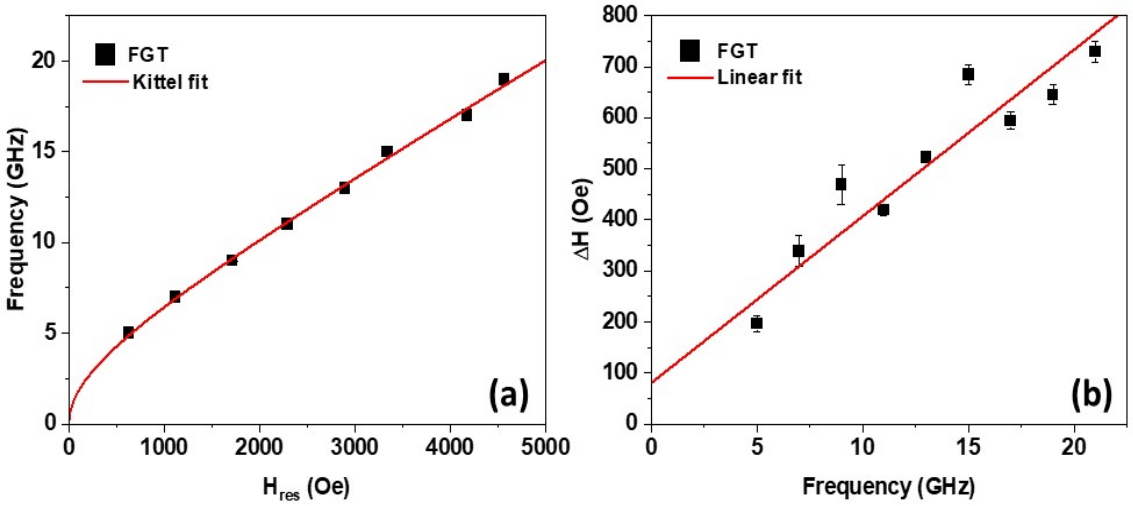

Fig. S14 (a) Frequency vs. resonant magnetic field dispersion acquired in the IP configuration for sample FGT (black squares). The red solid line indicates the fit of the dataset according to the Kittel equation by Eq. (1). (b) Evolution of the FMR peak broadening with excitation frequency.

References

1 L. Alahmed, B. Nepal, J. Macy, W. Zheng, B. Casas, A. Sapkota, N. Jones, A. R. M. Brahlek, W. Jin, M. Mahjouri-Samani, S. S.-L. Zhang, C. Mewes, L. Balicas, T. Mewes, and Peng Li, Magnetism and spin dynamics in room-temperature van der Waals magnet Fe_5GeTe_2, *2D Mater.*, 2021, **8**, 045030.

2 M. Farle, Ferromagnetic Resonance of Ultrathin Metallic Layers, *Reports Prog. Phys.*, 1998, **61**, 7, 755–826.

3 E. Montoya, T. McKinnon, A. Zamani, E. Girt, B. Heinrich, Broadband Ferromagnetic Resonance System and Methods for Ultrathin Magnetic Films, *Journal of Magnetism and Magnetic Materials*, 2014, **356**, 12–20.